Cyclic CO2 – H2O injection and residual trapping: implications for CO2 injection efficiency and storage security

Cyclic CO_2 – H_2O injection and residual trapping: implications for CO_2 injection efficiency and storage security

Edlmann K.[1], Hinchliffe S.[1], Heinemann N.[1], Johnson G.[1], Ennis-King J.[2] and McDermott C.I.[1]

[1]School of GeoSciences, University of Edinburgh, Grant Institute, The King's Buildings, University of Edinburgh, James Hutton Road, Edinburgh, EH9 3FE. United Kingdom.

[2]CSIRO Energy, Private Bag 10, Clayton South VIC 3169, Australia.

Corresponding Author

Katriona Edlmann: School of Geoscience, Grant Institute, The King's Buildings, University of Edinburgh, James Hutton Road, Edinburgh, EH9 3FE, United Kingdom.

kedlmann@staffmail.ed.ac.uk

Telephone: +44 (0) 131-650-7339

Fax: +44 (0) 131-668-3184

Graphical abstract

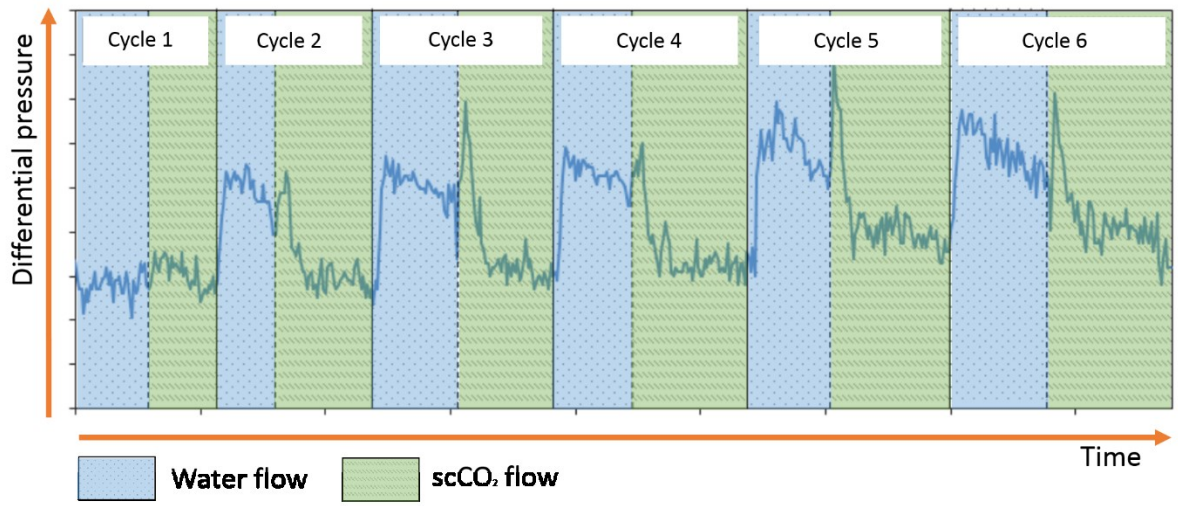

Abstract

To meet the Paris Agreement target of limiting global warming to 2ºC or below it is widely accepted that Carbon Capture and Storage (CCS) will have to be deployed at scale. For the first time, experiments have been undertaken over six cycles of water and supercritical CO_2 injection using a state of the art high flow rig recreating in-situ conditions of near wellbore injection into analogue storage reservoir rocks. The results show that differential pressure continuously increases over multiple injection cycles. Our interpretation is that multiple cycles of injection result in a reduced effective permeability due to increased residual trapping acting as a barrier to flow resulting in reduced injectivity. This is supported by numerical modelling and field observations that show CO_2 injectivity and its variation over time will be affected by multiple cycles of injection. These results suggest that loss of injectivity must be incorporated into the injection strategy and that careful management of cyclic injection will create the opportunity to increase residual trapping.

1. Introduction

The injection and storage of CO_2 into deep saline aquifers could make a significant contribution to reducing global greenhouse emissions (Bachu and Adams, 2003; Benson

and Cole, 2008; Edlmann et al., 2015; Heinemann et al., 2018; IEA, 2004; Koide et al., 1992; Metz, Davidson, de Coninck, 2005). Current field experience (Alcalde et al., 2017; Hosa et al., 2011) suggests that a single well can inject in excess of 1MT of CO_2 per year with numerical simulations indicating that during constant CO_2 injection, these injectivity rates can be maintained (Heath et al., 2014; Jikich et al., 2003; Rutqvist et al., 2008; Zoback and Gorelick, 2012). However, due to multiple input sources of CO_2, alternating CO_2 / brine injection strategies, periodic injection and varying injection rates along with well maintenance and workovers, a constant maintained injection strategy over a ~30 year project lifetime is unlikely. Field experience from CO_2-EOR projects using water alternating gas injection (WAG) have shown that a 20% loss of injectivity over the well life can be expected (Potter et al., 1992; Schneider and Owens, 1976; Sohrabi et al., 2005). This suggests that ensuring CO_2 injectivity can be maintained will require careful understanding of the fluid pressure response to cyclic injection over time (Burton et al., 2008). Fluid mobility has a direct impact on the injectivity of a well because fluid mobility is reduced in a multiphase system leading to higher fluid pressures (Bachu, 2008; Dullien, 1992; Edlmann et al., 2013; Heinemann et al., 2012; Morris et al., 2011). This means that to maintain injection rates higher pressures will be experienced, which is, however, limited by fracturing pressure, which if exceeded has the potential to open flow paths through which the CO_2 could escape (Edlmann et al., 2016; McDermott et al., 2013; Smart et al., 2001).

The limited cyclic CO_2 / water (or brine) injection experiments on the multiphase flow characteristics of CO_2 injection in the literature generally do not extend beyond two cycles (Edlmann et al., 2013; Gamadi et al., 2014; Grigg and Svec, 2006, 2007; Larsen A., 1995; Ma et al., 2016). Saeedi et al. undertook four cycles of injection and found that there were notable hysteresis effects on injectivity during cyclic CO_2 - brine injection (Saeedi et al., 2011). They suggested that this hysteresis effect may be limited to the first and second flooding cycles.

In this paper, we present the results of six cycles of CO_2 - brine injection. Our experiments have been designed using water unsaturated with respect to CO_2 to concentrate our focus on the near well bore injection area and in particular the response of the bottom hole / injection pressure. We find that for both the CO_2 and water injection cycles, the differential pressure increases with each injection cycle and that the hysteresis effect is progressive. Fluid mobility, which controls the differential pressure in the experiments, is influenced by (1) pore space geometry, (2) wettability characteristics, and (3) the residual saturation of each fluid phase. We investigate all three of these influences to determine which is responsible for the increase in differential pressure and confirm our interpretation by numerically simulating the experiments and by reviewing real-world CO_2 injection operations. The following sections present the equipment summary, the experimental methodology, fluid properties, sample characterisation, and the numerical simulation techniques. These have been designed to minimise the potential for the sample pore network and mineralogy to impart significant capillary pressure, mineral reactivity, clay mobilisation, wettability or thermal alteration influences that may be possible explanations for the changes in permeability. This enables us to suggest that the most likely explanation for the observed changes in permeability is changes in residual trapping during multiple cycles of CO_2 and water injection.

2. Materials and methods

The experimental rig was designed to recreate subsurface near wellbore CO_2 injection conditions. The equipment consists of a Hassler-type pressure vessel which holds cylindrical rock samples of 38mm diameter within a pressurised rubber sleeve that applies the confining pressure. A pair of Teledyne ISCO syringe pumps at the upstream end of the fluid system control the flow rate of CO_2 and a HPLC water pump controls the flow rate of water. A second pair of syringe pumps on the downstream end of the fluid system work in constant pressure mode to control the fluid pressure. The core holder is contained within an oven, allowing the temperature of the sample to be controlled and maintained. Full details of the experimental equipment and considerations are given in the Supporting Information (SI).

Saturation tracking and fluid collection was not possible within the experimental setup. To recreate subsurface injection conditions as closely as possible, the experiment was run with supercritical phase CO_2. To achieve this, the rock and fluid temperature was set to 40°C, the pore / fluid pressure at 10MPa, the confining pressure at 20MPa and the flow rate for both the water and CO_2 pumps set to 1ml/min.

2.1. Experimental methodology

After injecting water through the sample to steady state flow for at least 15 minutes (primary imbibition phase), the water injection is stopped and CO_2 injection initiated (primary drainage phase), maintaining steady state CO_2 injection for at least 15 minutes. The second cycle then begins by stopping the CO_2 injection and re-initiating the water injection (secondary imbibition phase), maintaining steady-state water injection for at least 15 minutes followed by CO_2 injection (secondary drainage phase), again maintaining steady state CO_2 injection for at least 15 minutes. This sequence was repeated for six cycles of alternating CO_2 and water injection. The detailed experimental process cycle for the flow experiments and the exact timings of the flow cycles are provided in the SI.

2.2. Fluid properties

The two fluids used during the cyclic experimental work were de-ionised water (unsaturated with respect to CO_2) as a proxy for brine and supercritical CO_2. The mass flow rate of water is in parity with the volumetric flow rate, assuming at 40°C and 10MPa the water density is 992.2kg/m^3 and dynamic viscosity is 6.53 x10^{-4}Pa.s (Suekane, 2008). The ISCO CO_2 syringe pump pressure was maintained at 10MPa and at a temperature of 5°C to ensure pump efficiency (CO_2 density of 947.3kg/m^3 at 10MPa and 5°C) therefore the mass flow rate leaving the pump is close to 1ml/min. However, the temperature of the CO_2 fluid entering the core sample passes through a heat exchanger at oven at 40°C where the CO_2 density is 628.7kg/m^3 at 10MPa with a dynamic viscosity of 4.82 x10^{-5}Pa.s. This results in a change in the volumetric flow rate through the sample. The flow rate of CO_2 through the sample was estimated using mass conservation from the pump mass flow rate (1ml/min) multiplied by the

density ratio of the syringe pump CO_2 over the sample inlet CO_2 (947.3 / 628.7 = 1.5), resulting in a volumetric flow rate for CO_2 into the sample of 1.5ml/min.

The solubility of CO_2 is controlled by temperature, pressure, and concentration of dissolved matter. Under the experimental conditions the CO_2 solubility is approximately 54.9kg per 1000kg of unsaturated water, so 1 pore volume of water can dissolve 0.087 pore volumes of CO_2.

2.3. Sample Characterisation

The experiment was conducted on Fell sandstone, a homogeneous quartz rich sandstone and suitable UK North Sea aquifer storage analogue (Heinemann et al., 2013; Lewicki et al., 2007; McDermott et al., 2017). It was chosen as it has an open pore network and is primarily composed of quartz, minimising the potential for significant capillary pressure or mineral reactivity influences, thereby enabling us to concentrate on the multiphase fluid response.

The experiment was conducted on a 38mm diameter and 80mm long cylindrical sample of Fell sandstone, with a helium porosity of 20.3%, implying a pore volume of 18.4ml. The sample intrinsic permeability to water of 26.24mD was measured at the beginning of the experiment. These porosity and permeability values correspond well to those encountered within the most likely UK and US CO_2 storage reservoir formations: Rotliegends (13 to 18% porosity and 76.8 to 322mD (Glennie, 1990)); Bunter sandstone (15 to 26% porosity and 100 to 700mD (Abbotts, 1991; Reynolds et al., 2018)); Deactur Mt Simon sandstone (13 to 22.4% porosity and 26.4mD to 1D permeability (Frailey et al., 2011)); Goldeneye Captain sandstone (~26% porosity and 1.1 to 7D permeability (McDermott et al., 2016; Reynolds et al., 2018)); Sleipner Utsira sandstone (27 to 42% porosity and 1-3D permeability (Chadwick et al., 2004)) and the Ormskirk sandstone (27% porosity and 0.0001 to >1D permeability (Meadows and Beach, 1993; Reynolds et al., 2018)).

2.3.1. Sample mineralogy

The mineralogical composition of the sandstone was determined using X-Ray Diffraction (XRD) before and after the experiment, supplemented by optical microscopy and Scanning Electron Microscope (SEM) investigations to assess whether there was chemical reactivity that could impact on the pore space geometry. The Fell sandstone is primarily quartz (93%) with microcline (2%), illite (1.2%), kaolinite (1%) and calcite (0.1%). Detailed SEM images and the XRD mineral abundances before and after the experiment are given in the SI.

2.3.2. Pore space geometry analysis

There is a large body of work that relates pore size and shape to capillary pressure, relative permeability and hysteresis, where capillary pressure decreases as pore throat radius increases (Dullien, 1992; Garcia et al., 2009; Jerauld and Salter, 1990; Pittman, 1992). Pore shape analysis of the Fell sandstone was calculated on four images over three magnifications obtained from the optical microscope (OM) and backscattered (BS) SEM images with the full results available in section 5 of the SI. The image analysis results show that the majority of the pores are between 100μm to 400μm in size. Gamma (γ) values for the Fell sandstone, which expresses the roundness of a pore, with 1 a perfect sphere and the pore space becomes increasingly complex and diverging as γ increases (Anselmetti, F.S., Luthi, 1998) are between 2 and 4 which indicates the pores are relatively simple and well rounded. γ increases as pore size increases suggesting the smaller pores are well-rounded becoming slightly more complex with increasing size. This implies that the influence of pore geometry does not inhibit fluid mobility, hence its influence on fluid flow characteristics will be minimal and will not significantly influence the effective permeability results. Full details of the pore space geometry analysis are presented in the SI.

2.4. Numerical simulation

Cyclic injection of different fluid phases will cause a hysteresis effect. Capillary forces within each of the drainage and imbibition cycles cause some of the non-wetting CO_2 to become disconnected, through snap-off, immobilised and residually trapped.

The first part of the numerical modelling fits a hysteretic model directly to the experimental data, in order to judge whether the observed behaviour fits within a standard paradigm. The hysteretic model for relative permeability and capillary pressure is outlined by Doughty (Doughty, 2007) and implemented in the inverse modelling code iTOUGH2 (Finsterle, 2004). The core is modelled as homogeneous cylinder of rock, and it is assumed that variations in saturation only occur along the axial direction i.e. the problem is one dimensional. The rates and timing of injection of water and CO_2 are taken directly from the experiment, and the model is fitted to experimental pressures at chosen calibration points (six per cycle) by adjusting the parameters of the hysteresis model through inversion algorithms.

It has been observed in core floods that due to the time scales of CO_2/water equilibration within the pore space relative to the flow velocity, the water that flows out of the core may be less than fully saturated with CO_2. Thus the standard assumption in the simulator of local equilibrium between phases may not reflect the experimental situation, and reduced dissolution could potentially lead to increasing CO_2 saturation across cycles. In these experiments there is no direct measurement of the concentration of CO_2 in the outflow and it is uncertain if the water injected during the experiments was fully saturated with CO_2 as it is simulated using the numerical simulators. The effect of this non-equilibrium in CO_2 and water dissolution can be partially mimicked in the simulations in a simple way by reducing the effective solubility of CO_2 in water. As a reference case, one simulation with a CO_2 solubility reduced to 50% of the bulk value at the experimental P, T conditions was run.

The second part of the numerical modelling examines whether the observed increase in differential pressure could be due to an enhancement of the hysteresis beyond the model

199 just discussed. An alternative model for CO_2 saturation has been devised in which the
200 residual gas saturation for imbibition is increased for each cycle. The reservoir engineering
201 software Eclipse 300 (Schlumberger) (Heinemann et al., 2016; Pickup et al., 2012), was
202 used in this study with the CO_2STORE option based on a modified Peng-Robinson equation
203 of state (Peng and Robinson, 1976) that allows for the mutual solubility of CO_2 and water.

204 Because it is the purpose of the simulations to show that the differential pressure increase
205 during cyclic CO_2 and water injection can be due to an increase in residual gas saturation,
206 mathematical relative permeability curves adopted from (van Genuchten, 1980) and (Corey,
207 1954) were used:

208 $$k_{rl} = \sqrt{S^*}\{1 - (1 - [S^*]^{1/m})^m\}^2 \quad [1]$$

209 $$k_{rg} = (1 - S')^2(1 - S'^2) \quad [2]$$

210 Where

211 $$S^* = (S_1 - S_{lr})/(1 - S_{lr}) \quad [3]$$

212 $$S' = (S_1 - S_{lr})/(1 - S_{lr} - S_{gr}) \quad [4]$$

213 The irreducible water saturation (S_{lr}) is initially set to 0.1, the residual gas saturation (S_{gr}) set
214 to 0.05 and the parameter *m* set to 0.6269 according to (Xu et al., 2003) for sand. To model
215 the hysteresis effect during the first injection cycle, the residual gas saturation for imbibition
216 (S_{gri}) was set to 0.2 and is then increased by 0.1 for each cycle (Figure 1). This systematic
217 increase is not based on experimental data or fitted to the increase in differential pressure
218 observed during the experiments described in this study. However, it shows that a stepwise
219 increase in residual gas saturation leads to an increase of the differential pressure. Capillary
220 pressure has been neglected.

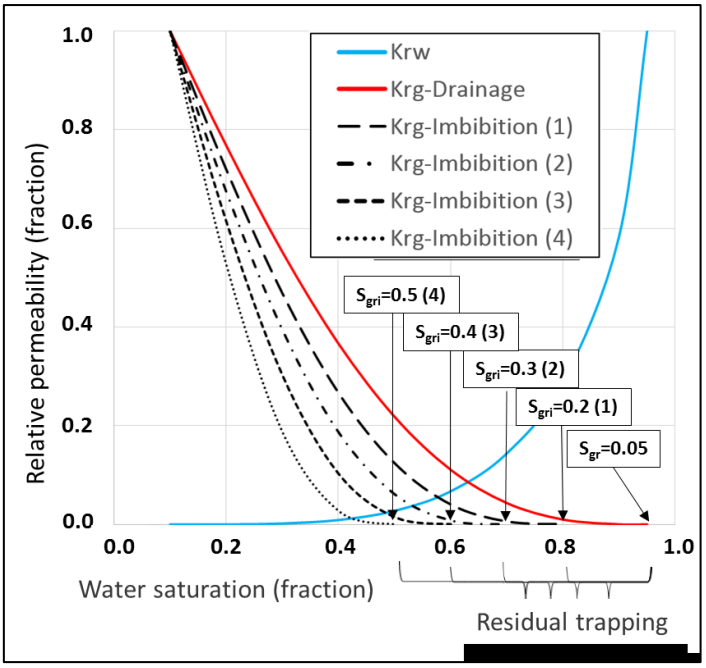

Figure 1 The relative permeability curves for water (krw – blue) and CO_2 (krg – red). The residual saturation for the imbibition process (Sgri) for the four modelled injection cycles increases with every cycle (the cycle number in brackets).

3. Results

3.1. Differential pressure evolution during cyclic CO_2 and water injection

Figure 2 presents the differential pressure response over all six $scCO_2$ / water flow cycle experiments. There is a progressive increase in differential pressure (reduction in fluid mobility) over the six cycles for both fluid phases. For the water phase, the average differential pressure nearly doubled from 5.6psi in cycle 1 to 11.3psi in cycle 6. For the $scCO_2$ phase, the average differential pressure increased from 6.3psi in cycle 1 to 8.1psi in cycle 6. Interestingly the water, which is considered to be the wetting phase, has a higher differential pressure than the $scCO_2$ and this is explored in more detail in Section 4.

Looking at the results of the water injection cycles (imbibition) in Figure 2 we see that after a $scCO_2$ injection cycle as water is injected there is a sharp increase in differential pressure (decrease in fluid mobility), followed by a slow reduction in differential pressure until the next cycle. For the $scCO_2$ injection cycles (drainage) we see that after a water injection cycle, as

238 $scCO_2$ is injected, there is a significant increase in differential pressure followed immediately
239 by a sharp fall in differential pressure (an increase in fluid mobility) to a differential pressure
240 below that of the previous water cycle. There is then no significant change in differential
241 pressure over each $scCO_2$ injection period, suggesting that once the $scCO_2$ is connected it
242 maintains a stable flow path.

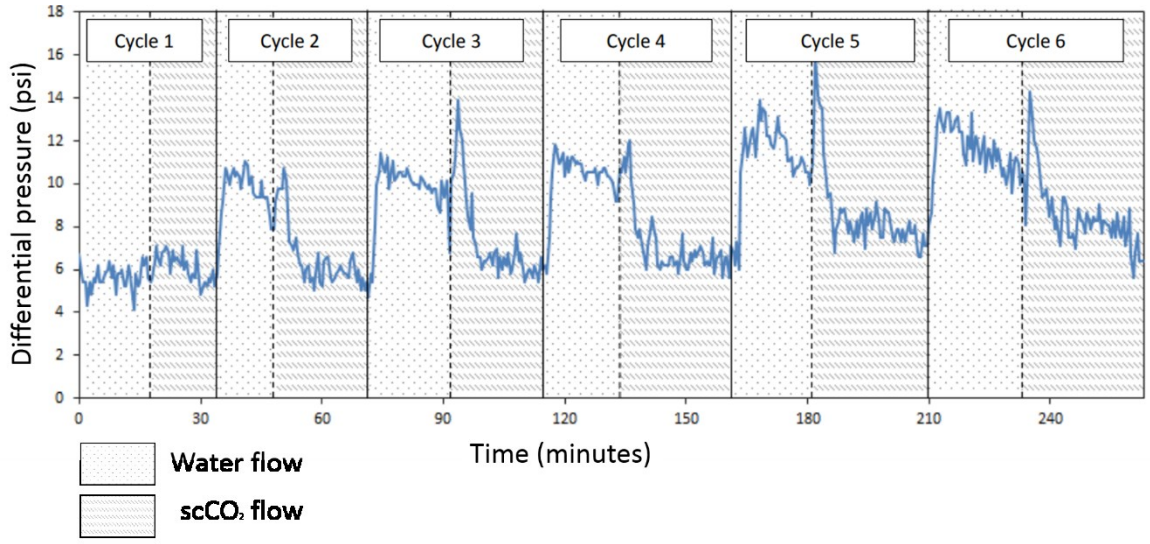

243

244 *Figure 2 Differential pressure results during cyclic flow for the Fell Sandstone sample. The*
245 *cycle number is indicated at the top of the graph. The relevant fluid flow within each cycle is*
246 *indicated in the key. The differential pressure response is plotted as a 5 point moving*
247 *average (which equates to a 30 second average) and more detail of this and the associated*
248 *errors are given in the SI.*

249 **3.2. Mineralogy and pore geometry analysis**

250 Full XRD and optical microscopy results for the Fell sandstone for both the pre and post
251 brine - CO_2 flooding experiments are presented in the SI. There is only a small amount of
252 reactive carbonates such as calcite (0.1%) which limits the potential for carbonate
253 dissolution processes within the rock. There are no swelling or reactive clays present (such
254 as montmorillonite) which could have an impact on the flow path of CO_2 by obstructing pore
255 throats through the remobilisation of fine clay particles within the limited timeframe of the
256 experiments (Dávila et al., 2017; Kampman et al., 2014). There are minor amounts of

kaolinite (1wt%) and Illite 1.3wt% which some researchers have shown will deflocculate or exhibit minor swelling in water or brine (Aksu et al., 2015; Baptist and Sweeney, 1947; Dodd et al., 1954; Leone and Scott, 1988). The sample preparation methodology of vacuum saturating the sample for a week prior to the experiments have been designed to minimise the impact of this potential swelling during the short duration experiments. The reduction in pH associated with CO_2 dissolution into the water during the experiment will further reduce the impact of any clay swelling, particularly in the kaolinite as the dispersion of clays is minimised at low pH (Mohan and Fogler, 1997; Mungan, 1965; Simon et al., 1976; Valdya and Fogler, 1992; van Oplhen H, 1964).

The post-experiment results show minor changes to some minerals after the flow experiments, but in all cases, the percentage mineral change is smaller than the presented standard deviation of the samples. Pre and post-experiment optical microscope photographs of the injection surface of the rock sample also show no mineralogical or thermal alteration within the samples. We conclude that there is minimal mineral reactivity or thermal alteration during the experiment that could alter the pore space, pore throat geometry and as such fluid response. This reinforces our interpretation that the pore geometry does not inhibit or restrict the fluid mobility, and as such, the differential pressure during cyclic CO_2 and water injection.

4. Discussion of results

Wettability is the tendency of one fluid to “wet” or adhere to the surface of a solid in the presence of another immiscible fluid, termed the wetting and non-wetting fluid phase respectively. Wettability can be quantified by determining the contact angle between the wetting fluid and the solid surface involved (Aarnes et al., 2009; Dullien, 1992) and therefore is a function of the rock mineralogy as well as the fluid. The capillary threshold pressure is the pressure that must be overcome before a non-wetting phase will penetrate and flow within the connected pore network and is dependent on the interfacial tension between the wetting and non-wetting fluids, the contact angle between the mineral and fluid phase and

the pore throat radius. When a non-wetting phase is injected into a system the differential pressure will increase until the capillary threshold pressure is exceeded. Once the capillary threshold pressure has been exceeded, a continuous migration pathway can be created through which the non-wetting phase can flow and the pressure will drop to an almost constant value. Therefore, the pressure response in the experiments presented here can be used to infer the wettability of the system and whether a change in wettability may be the cause of the increasing pressure observed over the 6 cycles.

Firstly, the magnitude of the differential pressure measured when injecting the two phases (CO_2 and water) could be used to infer the wettability with the lower differential pressure corresponding with the wetting phase. However, this may not be conclusively diagnostic due to other effects discussed below. Secondly, the rate of change of the differential pressure during the cycle can be used to determine the wetting phase of the experiment. Here, the rate of change of the differential pressure within each cycle can provide an indication of the multiphase flow properties of both the water and $scCO_2$ during each cycle. If the rock and fluid properties are constant, the changes in differential pressures during injection is controlled by capillary pressure and relative permeability. The permeability of one phase at any given location will depend on the saturation of the other phase present along with interactions with the pore network (Aarnes et al., 2009). If water is the wetting phase then in each water flow section, the rate of change of the differential pressure over that period should be faster than for the non-wetting fluid, e.g. CO_2. Lastly, if the wettability changes over time the rate of change in the pressure response in each individual cycle would also change. It has been shown in recent studies that the wettability of quartz surfaces can alter from a strongly water-wet system towards a less water-wet system in the presence of $scCO_2$ (Chiquet et al., 2007; Saraji et al., 2013). As the Fell sandstone is 93% quartz, the possibility of a change in wettability as the cause of the change in differential pressure during cyclic injection must thus be taken into account.

In these experiments we predict the water to be the wetting phase. A possible explanation for why the wetting fluid (water) has a higher differential pressure than the non-wetting $scCO_2$ within each cycle could be related to the viscosity difference between the two fluids. The $scCO_2$ is the more mobile phase as it has a lower viscosity (Bachu and Bennion, 2008). This could lead to highly non-uniform displacement of the water leading to channelling of $scCO_2$ through a few preferential flow paths (Saeedi et al., 2011) which could reduce the differential pressure of the $scCO_2$ flow through the samples.

Figure 3 shows the rate of change in pressure in each phase for each cycle. To minimise the effect of any experimental errors during the pump changeovers, the first and last minutes of each cycle were discounted from the rate of change calculations. The median time for each section was found and the ΔP was calculated for the selected time period either side of the median time and a trendline added with its gradient used to observe changes to the ΔP over time.

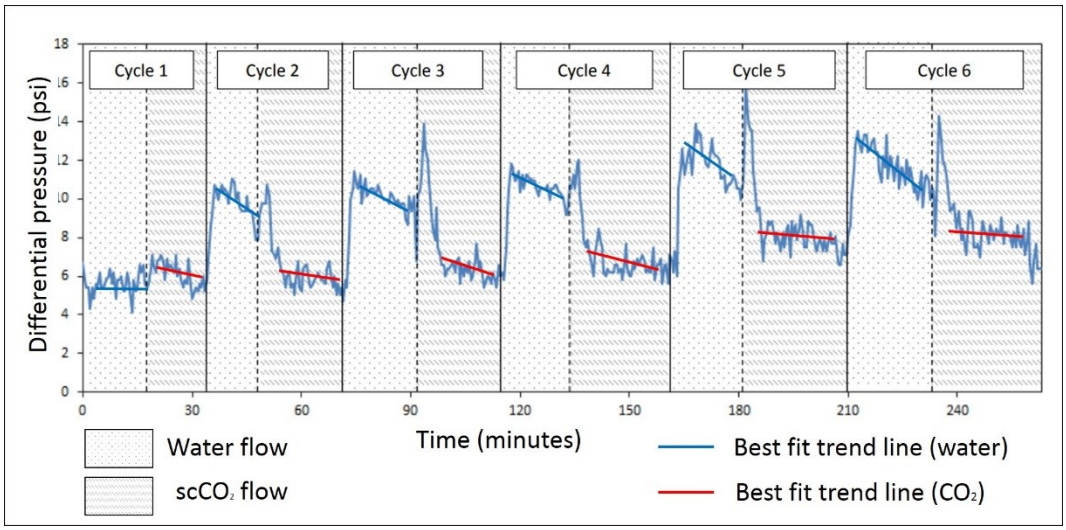

Figure 3 The rate of change in the differential pressure for each fluid flow over all six cycles.

Figure 2 shows that the reduction of the differential pressure during water injection is relatively steep whereas the pressure during CO_2 injection increases dramatically and then falls to a lower, barely changing level. This indicates that water is the wetting phase and CO_2 is the non-wetting phase throughout the experiments. It is therefore concluded from the rate

329 of change in pressure that the system is indeed water wet and that a wettability change from
330 water-wet to CO_2-wet is not responsible for the continuous increase in differential pressure
331 during cyclic water and CO_2 injection.

332 **4.1. Residual trapping**

333 Within a two-phase system the fraction of the pore space occupied by the wetting and non-
334 wetting phase is called the saturation, denoted S_w and S_{CO2} respectively:

335 $$S_w + S_{CO2} = 1 \qquad [5]$$

336 Where the non-wetting CO_2 phase can never reach either 0 or 1, due to the wetting water
337 phase adhering to the mineral surfaces. Hence, the two-phase system will actually range
338 from the critical water saturation S_{wc} to the maximum water saturation S_w^{max}.

339 If we consider the typical relative permeability function of water with respect to CO_2
340 saturation shown in Figure 1, it shows that the less CO_2 present, the higher the wetting
341 phase brine relative permeability, and vice versa. The curve shape is also dependant on flow
342 direction, whether it is undergoing drainage or imbibition. The curves are different as the
343 wetting and non-wetting phase take different flow paths through the network of pores.
344 During drainage the wetting fluid will preferentially fill the smaller pores and pore throats and
345 as the non-wetting fluid begins to flow as a continuous phase through the bigger pores,
346 occupying smaller pores as the non-wetting phase saturation increases. During this drainage
347 cycle, the wetting fluid (water) becomes increasingly reduced and eventually will be present
348 only as a thin film of residual water surrounding the edge of pores, termed irreducible water
349 saturation (S_{ir}). During the imbibition cycle when the wetting phase re-enters the pore
350 network, some of the non-wetting phase becomes gradually disconnected by the wetting
351 phase through capillary snap off and leads to residual trapping as the disconnected non-
352 wetting CO_2 become effectively immobile (Hesse et al., 2009). Each cycle imparts its own
353 change in the fluid saturation profile termed hysteresis (Juanes et al., 2006) which refers to
354 the dependence on the relative permeability to the previous saturation of the sample (Spiteri

and Juanes, 2006). Intuitively, as more and more non-wetting CO_2 phase enters through the pore volume, the harder it will be for the wetting water phase to push it all out, as more and more non-wetting CO_2 volume becomes trapped in the smaller pores.

If the injection cycle number is used as a proxy for decreasing water saturation in the core as a result of an increasing amount of residually trapped CO_2 within the pore network, we can create a proxy water relative permeability curve, full details are presented in the SI. The water relative permeability curve shows a gradual decrease in effective permeability with decreasing water saturation (increasing cycle number) which is consistent with the flow experiment results that indicate that with multiple water / CO_2 injection cycles, increased residual trapping acts as a barrier to flow and plays an important part in controlling multiphase fluid dynamics during cyclic water / CO_2 injection.

This is important as it indicates that over the lifetime of a storage site, experiencing natural cycles of fluid imbibition and drainage, the injectivity of the CO_2 may reduce over time, leading to lower injection rates and/ or increased reservoir pressures.

4.2. Residual saturation simulation analysis

For the first stage of simulation, Figure 4 shows the fitting of a hysteresis model with iTOUGH, where selected pressure points (shown as open circles) are used for the fit. The details of the fitting parameters and the hysteresis model are discussed in the SI. If the average data from just the first 4 cycles is used for the inverse model (solid green curve), then the fit is moderate for those cycles, mainly because the differential pressure in these cycles hardly changes in the experiments. However, when modelling the 5th and 6th cycle, where the experiments show a significant increase in differential pressure, the model doesn't capture the pressures increases, particularly during the CO_2 injection stages. Fitting to the average of all 6 cycles doesn't markedly improve the overall quality of fit, and the model is again unable to reproduce the increase in differential pressure over cycles – in each new cycle after the second one, the model gives a very similar result to the previous cycle. This

indicates that the hysteresis model is unable to capture some features of the behaviour for multiple injection cycles.

As discussed earlier, the effect of reduced effective solubility is also investigated, since during water imbibition there is dissolution of CO_2 as well as displacement. Injection of water for 30 minutes corresponds to 1.63 pore volumes, which could dissolve 0.14 pore volumes of CO_2 assuming full saturation. The fitted results with the effective solubility at 50% of the bulk value is shown as the dashed black curve. The pressure falloff during the water imbibition stages is flatter in this model (since less CO_2 is dissolved over the injection cycle), but this fails to improve the agreement with the experimental data, and indeed the fitted behaviour of the 3rd-6th cycles closely follows the 2nd cycle. Thus reduced effective solubility is unable to account for the observations.

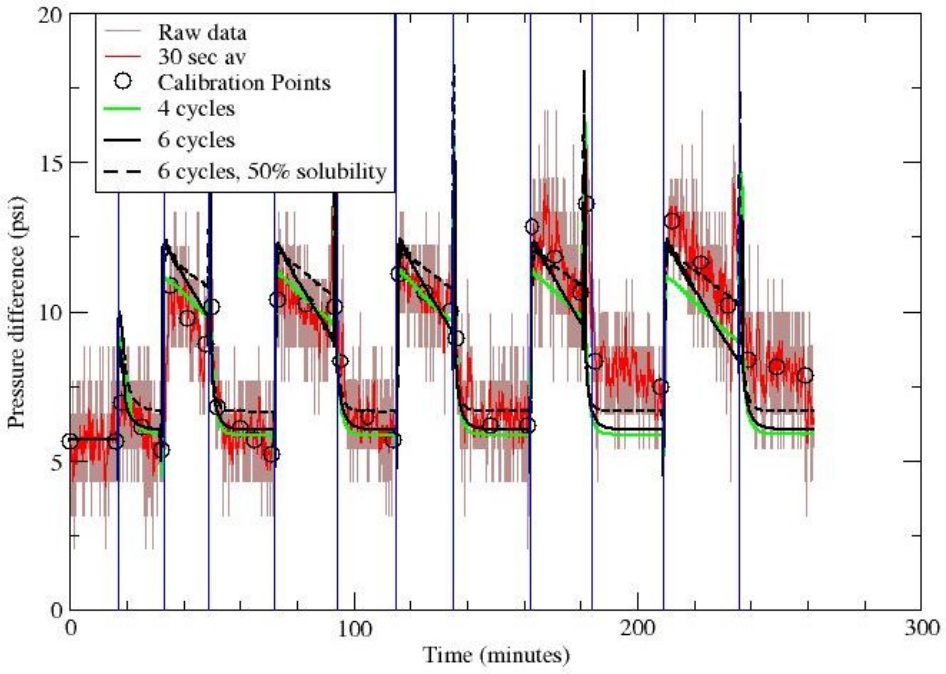

Figure 4 Fitting of the experimental results to a hysteresis model with iTOUGH2. Brown curve: The raw experimental data. Red curves: 30 second average of experimental data. Open circles: calibration points for fit. Solid green curve: hysteresis model fitted to just the first four cycles of water/CO_2 injection. Solid black curve: hysteresis model fitted to all six

cycles of water/CO_2 injection. Dashed black curve: hysteresis model fitted to all six cycles of water/CO_2 injection but with reduced effective solubility 50% of bulk value.

Saturation profiles along of the core are shown in Figure 5 for various points in the simulation. The CO_2 saturation is almost identical after each CO_2 injection cycle (only the profiles for the 1st and 6th cycles for clarity). When water is injected, there is a displacement of CO_2 down to a residual value, which depends on the initial saturation at each point, in accordance with the hysteresis model. There is also a dissolution front which moves along the core from the inlet, and which assumes instantaneous dissolution at the front as unsaturated water contacts CO_2. It can be seen in this Figure that the difference between the water injection cycles is mainly due to their duration, since water injection for a longer duration (e.g. the sixth cycle) propagates the dissolution front further from the inlet. Changing the effective solubility slows the propagation of the dissolution front (not shown here), so that it does not penetrate as far from the inlet over the duration of the water injection cycle.

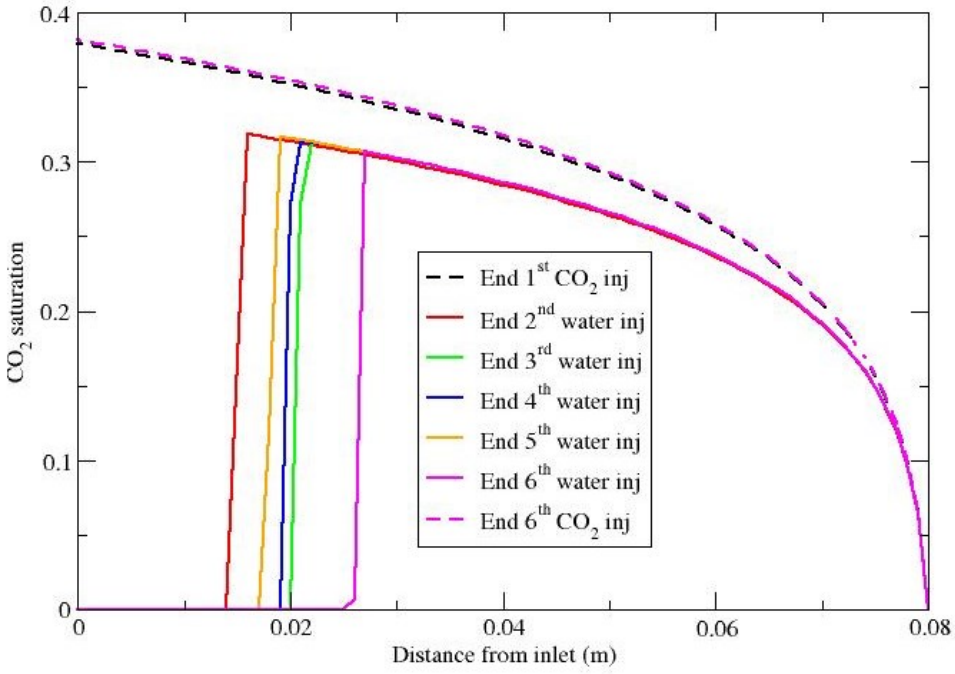

Figure 5 CO_2 saturation profiles along the core during the TOUGH2 simulation, Dashed black curve: end of 1st CO_2 injection. Solid red curve: end of 2nd water injection. Solid green curve: end of 3rd water injection. Solid blue curve: End of 4th water injection. Solid orange

curve: end of 5th water injection. Solid magenta curve: end of 6th water injection. Dashed magenta curve: end of 6th CO_2 injection.

The evolution of CO_2 saturation in the simulation at various locations in the core is shown in Figure 6. As seen in Figure 5 above, the saturation returns to the same level after each CO_2 injection. The next water injection then displaces CO_2 down to the residual saturation, which depends on the initial saturation according to the hysteresis model. Locations within 0.02 m of the inlet see the effect of the dissolution front during most of the water injection cycles, when the gas saturation falls to zero. This region of zero saturation near the inlet experiences no hysteresis on subsequent CO_2 injection. The fact that the CO_2 saturation profiles in Figure 5 are nearly the same after each CO_2 injection explains why the pressure response in the simulation to water injection is nearly the same in each cycle. This indicates that the hysteresis effects in the model are not sufficient to represent all the experimental observations

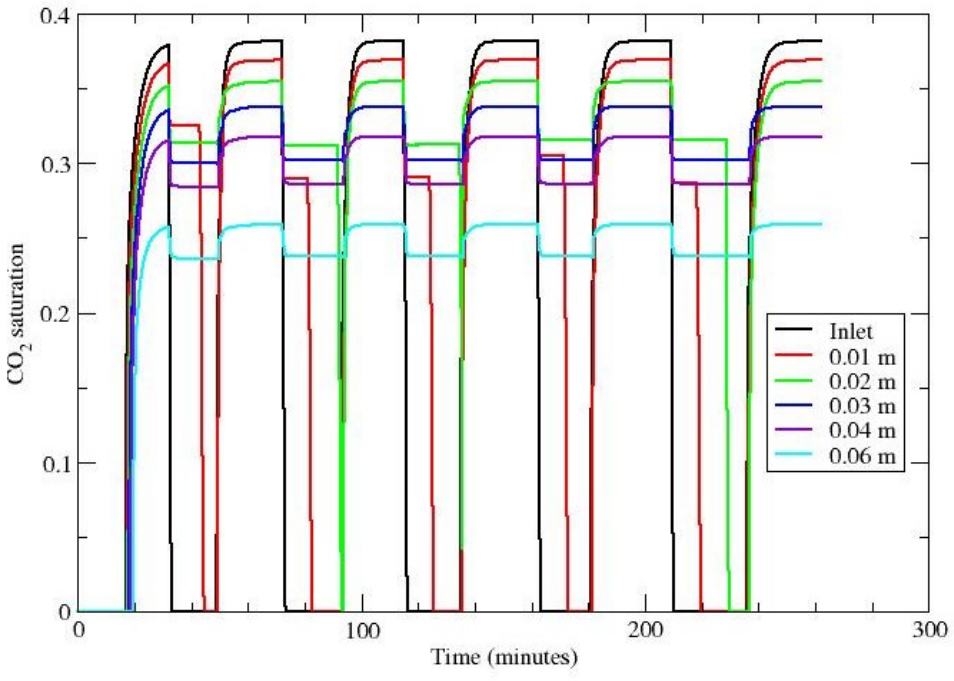

Figure 6 Evolution of CO2 saturation with time in the TOUGH2 simulation at fixed locations along the core, for the case fitted to the first 4 cycles of injection. Black line: Inlet. Red: 0.01 m from inlet. Green: 0.02 m. Blue: 0.03 m. Violet: 0.04m. Cyan: 0.06m.

The result of the second stage of modelling, in which the residual trapping in the model is deliberately increased between cycles (Figure 1), is shown in Figure 7. The comparison here is qualitative, in that the simulation model parameters have not been fitted to the data. Two similarities can be observed between the experimental results (Figure 2) and in the modelling results (Figure 7). Firstly, the absolute increase in differential pressure during the water injection period of cycles two, three and four, due to the increasing pore space occupied by residually trapped CO_2 which then has to be pushed out by the invading water. A greater or smaller increase in the residual saturation as the chosen 0.1 would lead to a greater or smaller increase in differential pressure, respectively. Secondly, the increasing rate of pressure decrease during the water injection period observed in the simulation results can also be seen in the experimental results.

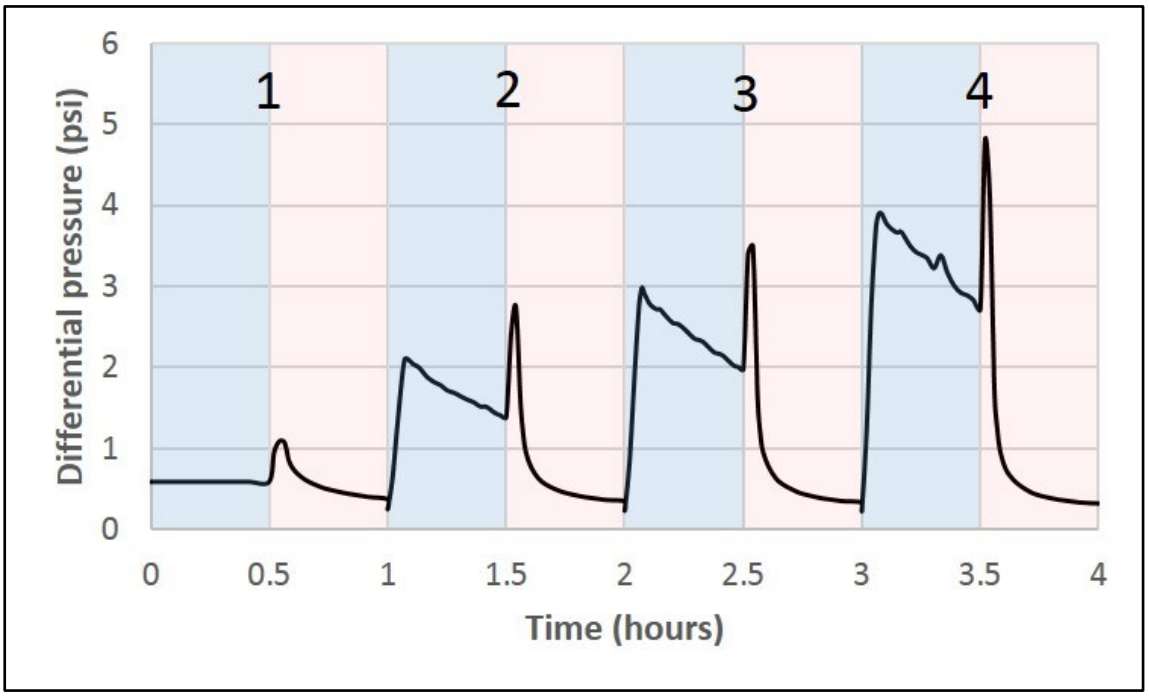

Figure 7 The differential pressure throughout the injection cycles. Periods of water injection are shaded in blue; periods of CO_2 injection are shaded in red. The cycle numbers are highlighted in black, the imbibition residual gas saturation increases with every cycle (see text for more information). Note the increase in differential pressure with increasing cycles.

449 The simulation results show that an increase in residual CO_2 trapping could lead to an
450 increase in differential pressure during the water injection period. Hence the simulation
451 results are evidence for the hypothesis that a continuous increase of residually trapped CO_2
452 is responsible for the increase in differential pressure, and indicate that alternative hysteresis
453 models may be needed to incorporate this behaviour in numerical simulations.

454 **4.3. Field observations**

455 Field observations of cyclic water and CO_2 injection are primarily in enhanced oil recovery
456 (EOR) projects where the third fluid phase (hydrocarbon) and production of fluids
457 complicates the interpretation of the pressure profiles as pertaining to residual CO_2 (Eshiet
458 and Sheng, 2014; Gamadi et al., 2014; Hovorka, 2013; Kampman et al., 2014; Meyer, 2005;
459 Müller, 2011). However, a number of field experiments have been performed in CO_2 – brine
460 only systems that allow comparison with the experimental and modelling data presented
461 here. One of these is the CO2CRC Otway experiment in Victoria, Australia. Here, an
462 engineered residual trapping experiment was conducted twice, once in 2011 and once in
463 2014 (Ennis-King et al., 2017). The field experiment design is discussed in detail by Zhang
464 et al. (Zhang et al., 2011) but in summary, consists of creating a residually trapped CO_2 zone
465 within the formation by following CO_2 injection with CO_2 saturated water injection. Here
466 pressure response was monitored throughout all stages of injection including during baseline
467 characterisation tests (pre CO_2 injection) (Ennis-King et al., 2017). Hence the comparison of
468 pressure profiles during water injection into a water-saturated only and residually trapped
469 CO_2 formation is possible. Figure 8 compares the pressure response to water injection
470 before residual CO_2 is present (1^{st} injection) and after it is present (2^{nd} injection) for both the
471 2011 and 2014 tests. Note that the since the injection rates were not the same each time,
472 the pressures have been scaled to allow a proper comparison. The presence of the residual
473 CO_2 phase significantly increases the pressure build-up which is attributed to the lower
474 relative permeability to water at residual CO_2 saturation. This observation concurs with the
475 results from the modelling and experimental work presented above. The difference between

476 the reservoir response in the 2011 and 2014 tests may be due to alteration of the near-well
477 permeability, possible from sand production (Ennis-King et al., 2017a).

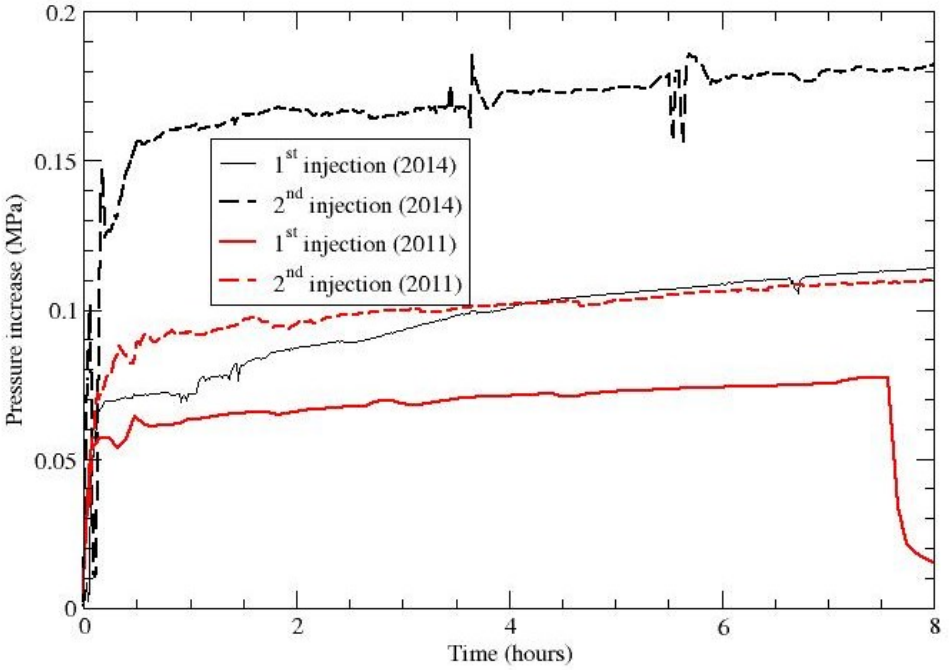

478

479 *Figure 8 Field data for pressure build-up during water injection before and after CO_2*
480 *injection. The single well test was carried out in 2011 and repeated in 2014. Since the*
481 *injection rates differ for each injection, the pressures have been scaled accordingly. Solid*
482 *black line: 1st injection (2014), 199 t/day (unscaled). Dashed black line: 2nd injection (2014),*
483 *rate 155 t/day, pressure scaled by 199/155. Solid red line: 1st injection (2011), 150 t/day,*
484 *pressure scaled by 199/150. Dashed red line: 2nd injection (2011), 191 t/day, pressure*
485 *scaled by 199/191.*

486 Modelling of enhanced trapping injection strategies including cyclic CO_2-water at the CO_2
487 field experiment in Israel (Heletz) (Rasmusson et al., 2016) is presented and discussed in
488 the SI, however, field results are not yet published so cannot be further compared here.

489

490

491

5. Conclusions

Our results clearly show, for the first time that the periodic injection of CO_2 over time may result in an increase in residually trapped CO_2. Our experiments and simulations are a direct analogue to deliberate operational changes (i.e. forced water injection) but they are equally applicable to periodic interruptions to CO_2 injection for example due to maintenance although this non forced imbibition (i.e. spontaneous water ingress with reduced injection pressure) may have a smaller effect than our experiments and simulations show. The results have implications that may benefit or hinder long-term CO_2 storage. On the one hand, increased residual trapping within the same pore space shows increased efficiency of storage operations and hence cost reductions (for example in monitoring a smaller areal footprint of CO_2 as compared to a plume of the same volume of CO_2 with lower saturations). Increased residual trapping also increases the storage security of an operation due to the reduced buoyant free-phase CO_2 that will be present. On the other hand, more residually trapped CO_2 in the vicinity of the well leads to more tortuous flow pathways for the injected CO_2 and hence to a pressure increase that may limit injectivity to within safe bounds. Hence a trade-off occurs between increased pore space utility and security of storage with injectivity and pressure increase. Our results thus will be of import to those deploying large scale and long-term storage and to those who regulate such operations.

6. Acknowledgements

The research leading to these results has received funding from the European Community's FP7 under grant agreement No. 227286, from the European Union's H2020 under Grant Agreement No. 636811, from the European Union's H2020 Accelerating CCS technologies, EPSRC Grant EP/P026214/1 and Data from Stage 2B of the Otway Pilot project has been provided by CO2CRC Ltd, and the field project had support from the Australian National Low Emissions Coal Research and Development (ANLEC R&D). We also gratefully acknowledge the input of our two anonymous reviewers.

7. Supporting information

The supporting information contains further detailed information on the experimental equipment, considerations, and processes. The sample mineralogy and pore space geometry analysis. The experimental relative permeability, residual saturation hysteresis, model and fitting parameters and details of other field examples with CO_2 cyclic flow.

8. References

Aarnes, J.E., Lie, K.-A., Kippe, V., Krogstad, S., 2009. Multiscale methods for subsurface flow, Multiscale modeling and …. https://doi.org/https://doi.org/10.1007/978-3-540-88857-4_1

Abbotts, I.L., 1991. United Kingdom oil and gas fields : 25-years commemorative volume. Geological Society.

Aksu, I., Bazilevskaya, E., Karpyn, Z.T., 2015. Swelling of clay minerals in unconsolidated porous media and its impact on permeability. GeoResJ 7, 1–13. https://doi.org/10.1016/J.GRJ.2015.02.003

Alcalde, J., Flude, S., Wilkinson, M., Johnson, G., Edlmann, K., Bond, C., Scott, V., Gilfillan, S., Ogaya, X., Haszeldine, R., 2017. Quantifying geological CO2 storage security to deliver on climate mitigation. Nat. Commun. Curr. Rev. https://doi.org/10.17605/OSF.IO/X59QG

Anselmetti, F.S., Luthi, S. and E.G.P., 1998. Quantitative Characterization of Carbonate Pore Systems by Digital Image Analysis. Am. Assoc. Pet. Geol. Bull. 10, 1815–1836. https://doi.org/10.1306/1D9BD155-172D-11D7-8645000102C1865D

Bachu, S., 2008. CO2 storage in geological media: Role, means, status and barriers to deployment. Prog. Energy Combust. Sci. 34, 254–273. https://doi.org/10.1016/j.pecs.2007.10.001

Bachu, S., Adams, J.J., 2003. Sequestration of CO2 in geological media in response to

543 climate change: Capacity of deep saline aquifers to sequester CO2 in solution. Energy
544 Convers. Manag. 44, 3151–3175. https://doi.org/10.1016/S0196-8904(03)00101-8

545 Bachu, S., Bennion, B., 2008. Effects of in-situ conditions on relative permeability
546 characteristics of CO2-brine systems. Environ. Geol. 54, 1707–1722.
547 https://doi.org/10.1007/s00254-007-0946-9

548 Baptist, O.C., Sweeney, S.A., 1947. The effect of clays on the permeability of reservoir
549 sands to waters of different saline contents.

550 Benson, S.M., Cole, D.R., 2008. CO2 sequestration in deep sedimentary formations.
551 Elements 4, 325–331. https://doi.org/10.2113/gselements.4.5.325

552 Burton, M., Kumar, N., Bryant, S.L., 2008. Time-Dependent Injectivity During CO2 Storage in
553 Aquifers. SPE/DOE Fourteenth Symp. Improv. Oil Recover. Tulsa, Oklahoma, USA 19--
554 23 April 19–23. https://doi.org/10.2118/113937-MS

555 Chadwick, R.., Zweigel, P., Gregersen, U., Kirby, G.., Holloway, S., Johannessen, P.., 2004.
556 Geological reservoir characterization of a CO2 storage site: The Utsira Sand, Sleipner,
557 northern North Sea. Energy 29, 1371–1381.
558 https://doi.org/10.1016/J.ENERGY.2004.03.071

559 Chiquet, P., Broseta, D., Thibeau, S., 2007. Wettability alteration of caprock minerals by
560 carbon dioxide. Geofluids 7, 112–122. https://doi.org/10.1111/j.1468-
561 8123.2007.00168.x

562 Corey, A.T., 1954. The Interrelation Between Gas and Oil Relative Permeabilites, Producers
563 Monthly.

564 Dávila, G., Cama, J., Luquot, L., Soler, J.M., Ayora, C., 2017. Experimental and modeling
565 study of the interaction between a crushed marl caprock and CO2-rich solutions under
566 different pressure and temperature conditions. Chem. Geol. 448, 26–42.
567 https://doi.org/10.1016/j.chemgeo.2016.10.034

568 Dodd, C.G., Conley, F.R., Barnes, P.M., 1954. Clay minerals in petroleum reservoir sands
569 and water sensitivity effects. https://doi.org/10.1346/CCMN.1954.0030118

570 Doughty, C., 2007. Modeling geologic storage of carbon dioxide: Comparison of non-
571 hysteretic and hysteretic characteristic curves. Energy Convers. Manag. 48, 1768–
572 1781. https://doi.org/10.1016/J.ENCONMAN.2007.01.022

573 Dullien, F.A.L., 1992. Porous media : fluid transport and pore structure. Academic Press.

574 Edlmann, K., Bensabat, J., Niemi, A., Haszeldine, R.S., McDermott, C.I., 2016. Lessons
575 learned from using expert elicitation to identify, assess and rank the potential leakage
576 scenarios at the Heletz pilot CO2 injection site. Int. J. Greenh. Gas Control 49, 473–
577 487. https://doi.org/10.1016/j.ijggc.2016.02.018

578 Edlmann, K., Edwards, M.A., Qiao, X.J., Haszeldine, R.S., McDermott, C.I., 2015. Appraisal
579 of global CO2 storage opportunities using the geomechanical facies approach. Environ.
580 Earth Sci. 73, 8075–8096. https://doi.org/10.1007/s12665-014-3965-3

581 Edlmann, K., Haszeldine, S., McDermott, C.I.I., 2013. Experimental investigation into the
582 sealing capability of naturally fractured shale caprocks to supercritical carbon dioxide
583 flow. Environ. Earth Sci. 70, 3393–3409. https://doi.org/10.1007/s12665-013-2407-y

584 Ennis-King, J., LaForce, T., Paterson, L., Black, J.R., Vu, H.P., Haese, R.R., Serno, S.,
585 Gilfillan, S., Johnson, G., Freifeld, B., Singh, R., 2017a. Stepping into the Same River
586 Twice: Field Evidence for the Repeatability of a CO2 Injection Test. Energy Procedia
587 114, 2760–2771. https://doi.org/10.1016/J.EGYPRO.2017.03.1392

588 Ennis-King, J., Laforce, T., Paterson, L., Dance, T., Jenkins, C., Cinar, Y., 2017b.
589 Interpretation of above zone and storage zone pressure responses to carbon dioxide
590 injection in the 2016 CO2CRC field test . Energy Procedia 114, 5671–5679.
591 https://doi.org/10.1016/j.egypro.2017.03.1706

592 Eshiet, K., Sheng, Y., 2014. Investigation of geomechanical responses of reservoirs induced

593 by carbon dioxide storage. Environ. Earth Sci. 71, 3999–4020.
594 https://doi.org/10.1007/s12665-013-2784-2

595 Finsterle, S., 2004. Multiphase Inverse Modeling. Vadose Zo. J. 3, 747.
596 https://doi.org/10.2136/vzj2004.0747

597 Frailey, S.M., Damico, J., Leetaru, H.E., 2011. Reservoir characterization of the Mt. Simon
598 Sandstone, Illinois Basin, USA. Energy Procedia 4, 5487–5494.
599 https://doi.org/10.1016/J.EGYPRO.2011.02.534

600 Gamadi, T.D., Sheng, J.J., Soliman, M.Y., Menouar, H., Watson, M.C., Emadibaladehi, H.,
601 2014. An Experimental Study of Cyclic CO2 Injection to Improve Shale Oil Recovery, in:
602 SPE Improved Oil Recovery Symposium. Society of Petroleum Engineers.
603 https://doi.org/10.2118/169142-MS

604 Garcia, X., Akanji, L.T., Blunt, M.J., Matthai, S.K., Latham, J.P., 2009. Numerical study of the
605 effects of particle shape and polydispersity on permeability. Phys. Rev. E - Stat.
606 Nonlinear, Soft Matter Phys. 80, 1–9. https://doi.org/10.1103/PhysRevE.80.021304

607 Glennie, K.W., 1990. Introduction to the petroleum geology of the North Sea. Blackwell
608 Scientific Publications.

609 Grigg, R., Svec, R., 2006. CO2 Transport Mechanisms in CO2/Brine Coreflooding. Proc.
610 SPE Annu. Tech. Conf. Exhib. https://doi.org/10.2118/103228-MS

611 Grigg, R.B., Svec, R.K., 2007. CO2 retention and injectivity changes : laboratory tests. Sixth
612 Annu. Conf. Carbon Capture Sequestration.

613 Heath, J.E., McKenna, S.A., Dewers, T.A., Roach, J.D., Kobos, P.H., 2014. Multiwell CO2
614 injectivity: Impact of boundary conditions and brine extraction on geologic CO2 storage
615 efficiency and pressure buildup. Environ. Sci. Technol. 48, 1067–1074.
616 https://doi.org/10.1021/es4017014

617 Heinemann, N., Booth, M.G., Haszeldine, R.S., Wilkinson, M., Scafidi, J. , Edlmann, K.,

618 2018. Hydrogen storage in porous geological formations – Onshore play opportunities
619 in the Midland Valley (Scotland, UK). https://doi.org/10.31223/osf.io/m4uw

620 Heinemann, N., Stewart, R.J., Wilkinson, M., Pickup, G.E.E., Haszeldine, R.S.S., 2016.
621 Hydrodynamics in subsurface CO2 storage: Tilted contacts and increased storage
622 security. Int. J. Greenh. Gas Control 54, 322–329.
623 https://doi.org/10.1016/j.ijggc.2016.10.003

624 Heinemann, N., Wilkinson, M., Haszeldine, R.S., Fallick, A.E., Pickup, G.E., 2013. CO2
625 sequestration in a UK North Sea analogue for geological carbon storage. Geology 41,
626 411–414. https://doi.org/10.1130/G33835.1

627 Heinemann, N., Wilkinson, M., Pickup, G.E., Haszeldine, R.S., Cutler, N.A., 2012. CO 2
628 storage in the offshore UK Bunter Sandstone Formation. Int. J. Greenh. Gas Control 6,
629 210–219. https://doi.org/10.1016/j.ijggc.2011.11.002

630 Hesse, M.A., Orr, F.M., Tchelepi, H.A., 2009. Gravity currents with residual trapping. Energy
631 Procedia 1, 3275–3281. https://doi.org/10.1016/j.egypro.2009.02.113

632 Hosa, A., Esentia, M., Stewart, J., Haszeldine, S., 2011. Injection of CO2 into saline
633 formations: Benchmarking worldwide projects.
634 https://doi.org/10.1016/j.cherd.2011.04.003

635 Hovorka, S.D., 2013. EOR as Sequestration — Geoscience Perspective.

636 IEA, 2004. Energy Technology Analysis: Prospects for CO2 Capture and Storage.
637 https://doi.org/10.1016/B978-1-85617-710-8.00010-8

638 Jerauld, G.R., Salter, S.J., 1990. The Effect of Pore Structure on Hysteresis in Relative
639 Permeability and Capillary Pressure: Pore Level Modeling. Transp. Porous Media 5,
640 103.

641 Jikich, S. a., Sams, W.N., Bromhal, G., Pope, G., Gupta, N., Smith, D.H., 2003. Carbon
642 dioxide injectivity in brine reservoirs using horizontal wells. Second Annu. Conf. carbon

643 sequestration, Dev. validating Technol. base to reduce carbon intensity, Alexandria,
644 Virginia 5–8.

645 Juanes, R., Spiteri, E.J., Orr, F.M., Blunt, M.J., 2006. Impact of relative permeability
646 hysteresis on geological CO2 storage. Water Resour. Res. 42, 1–13.
647 https://doi.org/10.1029/2005WR004806

648 Kampman, N., Bickle, M., Wigley, M., Dubacq, B., 2014. Fluid flow and CO2-fluid-mineral
649 interactions during CO2-storage in sedimentary basins. Chem. Geol. 369, 22–50.
650 https://doi.org/10.1016/j.chemgeo.2013.11.012

651 Koide, H., Tazaki, Y., Noguchi, Y., Nakayama, S., Iijima, M., Ito, K., Shindo, Y., 1992.
652 Subterranean containment and long-term storage of carbon dioxide in unused aquifers
653 and in depleted natural gas reservoirs. Energy Convers. Manag. 33, 619–626.
654 https://doi.org/10.1016/0196-8904(92)90064-4

655 Larsen A., J.A.. S., 1995. Comparing Hysteresis Models for Relative Permeability in WAG
656 Studies, Sca.

657 Leone, J.A., Scott, M.E., 1988. Characterization and Control of Formation Damage During
658 Waterflooding of a High-Clay-Content Reservoir. SPE Reserv. Eng. 3, 1279–1286.
659 https://doi.org/10.2118/16234-PA

660 Lewicki, J.L., Birkholzer, J., Tsang, C.F., 2007. Natural and industrial analogues for leakage
661 of CO2 from storage reservoirs: Identification of features, events, and processes and
662 lessons learned. Environ. Geol. 52, 457–467. https://doi.org/10.1007/s00254-006-0479-
663 7

664 Ma, J., Wang, X., Gao, R., Zeng, F., Huang, C., Tontiwachwuthikul, P., Liang, Z., 2016.
665 Study of cyclic CO2 injection for low-pressure light oil recovery under reservoir
666 conditions. Fuel 174, 296–306. https://doi.org/10.1016/J.FUEL.2016.02.017

667 McDermott, C., Williams, J., Tucker, O., Jin, M., Mackay, E., Edlmann, K., Haszeldine,

R.S.S., Wang, W., Kolditz, O., Akhurst, M., 2016. Screening the geomechanical stability (thermal and mechanical) of shared multi-user CO2 storage assets: A simple effective tool applied to the Captain Sandstone Aquifer. Int. J. Greenh. Gas Control 45, 43–61. https://doi.org/10.1016/j.ijggc.2015.11.025

McDermott, C.I., Miocic, J.M., Edlmann, K., Gilfillan, S.M.V., 2017. Natural analogue studies, in: Theory and Applications of Transport in Porous Media. https://doi.org/10.1007/978-94-024-0996-3_9

McDermott, C.I.I., Edlmann, K., Haszeldine, R.S.S., 2013. Predicting hydraulic tensile fracture spacing in strata-bound systems. Int. J. Rock Mech. Min. Sci. 63, 39–49. https://doi.org/10.1016/j.ijrmms.2013.06.004

Meadows, N.S., Beach, A., 1993. Controls on reservoir quality in the Triassic Sherwood Sandstone of the Irish Sea, in: Petroleum Geology of Northwest Europe: Proceedings of the 4th Conference. Geological Society of London, pp. 823–833. https://doi.org/10.1144/0040823

Metz, Davidson, de Coninck, L. and M., 2005. CARBON DIOXIDE CAPTURE AND STORAGE. Cambridge University press, New york.

Meyer, J.P., 2005. Summary of Carbon Dioxide Enhanced Oil Recovery (CO 2 EOR)Injection Well Technology Supporting. Am. Pet. Inst. 63. https://doi.org/http://www.api.org/~/media/Files/EHS/climate-change/Summary-carbon-dioxide-enhanced-oil-recovery-well-tech.pdf

Mohan, K.K., Fogler, H.S., 1997. Effect of pH and Layer Charge on Formation Damage in Porous Media Containing Swelling Clays.

Morris, J.P., Detwiler, R.L., Friedmann, S.J., Vorobiev, O.Y., Hao, Y., 2011. The large-scale geomechanical and hydrogeological effects of multiple CO2 injection sites on formation stability. Int. J. Greenh. Gas Control 5, 69–74.

https://doi.org/10.1016/j.ijggc.2010.07.006

Müller, N., 2011. Supercritical CO2-Brine Relative Permeability Experiments in Reservoir Rocks-Literature Review and Recommendations. Transp. Porous Media 87, 367–383. https://doi.org/10.1007/s11242-010-9689-2

Mungan, N., 1965. Permeability Reduction Through Changes in pH and Salinity. J. Pet. Technol. 17, 1449–1453. https://doi.org/10.2118/1283-PA

Peng, D.Y., Robinson, D.B., 1976. A New Two-Constant Equation of State. Ind. Eng. Chem. Fundam. 15, 59–64. https://doi.org/10.1021/i160057a011

Pickup, G.E., Mackay, E.J., Heinemann, N., Shariatipour, S.M., 2012. Flow simulation of CO 2 storage in saline aquifers using a black oil simulator. Carbon Manag. Technol. Conf. [CMTC] (Orlando, FL, 2/7-9/2012) Proc. 1, 276–289. https://doi.org/10.7122/151042-MS

Pittman, E.D., 1992. Relationship of porosity and permeability to various parameters derived from mercury injection-capillary pressure curves for sandstone. Am. Assoc. Pet. Geol. Bull. https://doi.org/10.1017/CBO9781107415324.004

Potter, G.F., Hadlow, R.E., Surguchev, L., Research, R., Korbel, R., Haugen, S., Krakstad, O., Patel, P.D., Christman, P.G., Gardner, J.W., 1992. Update of Industry Experience With CO2 Injection. SPE Annu. Tech. Conf. Exhib. 2, 507–513. https://doi.org/10.2118/25075-MS

Rasmusson, K., Rasmusson, M., Tsang, Y., Niemi, A., 2016. A simulation study of the effect of trapping model, geological heterogeneity and injection strategies on CO2 trapping. Int. J. Greenh. Gas Control 52, 52–72. https://doi.org/10.1016/J.IJGGC.2016.06.020

Reynolds, C.A., Blunt, M.J., Krevor, S., 2018. Multiphase Flow Characteristics of Heterogeneous Rocks From CO_2 Storage Reservoirs in the United Kingdom. Water Resour. Res. 54, 729–745. https://doi.org/10.1002/2017WR021651

718 Rutqvist, J., Birkholzer, J.T., Tsang, C.F., 2008. Coupled reservoir-geomechanical analysis
719 of the potential for tensile and shear failure associated with CO2 injection in
720 multilayered reservoir-caprock systems. Int. J. Rock Mech. Min. Sci. 45, 132–143.
721 https://doi.org/10.1016/j.ijrmms.2007.04.006

722 Saeedi, A., Rezaee, R., Evans, B., Clennell, B., 2011. Multiphase flow behaviour during CO2
723 geo-sequestration: Emphasis on the effect of cyclic CO2-brine flooding. J. Pet. Sci.
724 Eng. 79, 65–85. https://doi.org/10.1016/j.petrol.2011.07.007

725 Saraji, S., Goual, L., Piri, M., Plancher, H., 2013. Wettability of supercritical carbon
726 dioxide/water/quartz systems: Simultaneous measurement of contact angle and
727 interfacial tension at reservoir conditions. Langmuir 29, 6856–6866.
728 https://doi.org/10.1021/la3050863

729 Schneider, F.N., Owens, W.W., 1976. Relative Permeability Studies of Gas-Water Flow
730 Following Solvent Injection in Carbonate Rocks. Soc. Pet. Eng. J. 16, 23–30.
731 https://doi.org/10.2118/5554-PA

732 Simon, D.E., McDaniel, B.W., Coon, R.M., 1976. Evaluation of Fluid pH Effects on Low
733 Permeability Sandstones, in: SPE Annual Fall Technical Conference and Exhibition.
734 Society of Petroleum Engineers. https://doi.org/10.2118/6010-MS

735 Smart, B.G.D., Somerville, J.M., Edlman, K., Jones, C., 2001. Stress sensitivity of fractured
736 reservoirs. J. Pet. Sci. Eng. 29, 29–37. https://doi.org/10.1016/S0920-4105(00)00088-7

737 Sohrabi, M., Danesh, A., Tehrani, D., 2005. Oil Recovery by Near-Miscible SWAG Injection.
738 Proc. SPE Eur. Annu. Conf. 24–26. https://doi.org/10.2523/94073-MS

739 Spiteri, E.J., Juanes, R., 2006. Impact of relative permeability hysteresis on the numerical
740 simulation of WAG injection. J. Pet. Sci. Eng. 50, 115–139.
741 https://doi.org/10.1016/j.petrol.2005.09.004

742 Suekane, 2008. Geological storage of carbon dioxide by residual gas and solubility trapping.

743 Int. J. Greenh. Gas Control 2, 58–64. https://doi.org/10.1016/S1750-5836(07)00096-5

744 Valdya, R.N., Fogler, H.S., 1992. Fines Migration and Formation Damage: Influence of pH
745 and Ion Exchange. SPE Prod. Eng. 7, 325–330. https://doi.org/10.2118/19413-PA

746 van Genuchten, M.T., 1980. A Closed-form Equation for Predicting the Hydraulic
747 Conductivity of Unsaturated Soils1. Soil Sci. Soc. Am. J. 44, 892.
748 https://doi.org/10.2136/sssaj1980.03615995004400050002x

749 van Oplhen H, 1964. An introduction to clay colloid chemistry. By H van Olphen. Interscience
750 Publishers, Div. of John Wiley & Sons, 605 Third Ave., New York 16, N. Y, 1963.
751 xvi + 301 pp. 15.5 × 23 cm. Price $10, Journal of Pharmaceutical Sciences. Elsevier.
752 https://doi.org/10.1002/JPS.2600530238

753 Xu, T., Apps, J.A., Pruess, K., 2003. Reactive geochemical transport simulation to study
754 mineral trapping for CO_2 disposal in deep arenaceous formations. J. Geophys. Res.
755 Solid Earth 108, 1–66. https://doi.org/10.1029/2002JB001979

756 Zhang, Y., Freifeld, B., Finsterle, S., Leahy, M., Ennis-King, J., Paterson, L., Dance, T.,
757 2011. Single-well experimental design for studying residual trapping of supercritical
758 carbon dioxide. Int. J. Greenh. Gas Control. Elsevier Ltd.
759 https://doi.org/10.1016/j.ijggc.2010.06.011

760 Zoback, M.D., Gorelick, S.M., 2012. Earthquake triggering and large-scale geologic storage
761 of carbon dioxide. Proc. Natl. Acad. Sci. 109, 10164–10168.
762 https://doi.org/10.1073/pnas.1202473109

763